SANDIA REPORT
SAND2019-13408
Printed October, 2019

Sandia National Laboratories

Validation of the AltRAM physics models for use with compressed natural gas

Cyrus J. Jordan
North Carolina State University, Raleigh, NC

Ethan S. Hecht, and Myra L. Blaylock

Prepared by
Sandia National Laboratories
Albuquerque, New Mexico 87185
Livermore, California 94550

Issued by Sandia National Laboratories, operated for the United States Department of Energy by National Technology & Engineering Solutions of Sandia, LLC.

Available to DOE and DOE contractors from

U.S. Department of Energy
Office of Scientific and Technical Information
P.O. Box 62
Oak Ridge, TN 37831

Telephone: (865) 576-8401
Facsimile: (865) 576-5728
E-Mail: reports@osti.gov
Online ordering: http://www.osti.gov/scitech

Available to the public from

U.S. Department of Commerce
National Technical Information Service
5301 Shawnee Road
Alexandria, VA 22312

Telephone: (800) 553-6847
Facsimile: (703) 605-6900
E-Mail: orders@ntis.gov
Online order: https://classic.ntis.gov/help/order-methods

ABSTRACT

The Alternative Fuels Risk Assessment Models (AltRAM) toolkit combines Quantitative Risk Assessment (QRA) with simulations of unignited dispersion, ignited turbulent diffusion flames, and indoor accumulation with delayed ignition of fuels. The models of the physical phenomena need to be validated for each of the fuels in the toolkit. This report shows the validation for methane which is being used as a surrogate for natural gas.

For the unignited dispersion model, seven previously published experiments from credible sources were used to validate. The validation looked at gas concentrations with respect to the distance from the release point. Four of these were underexpanded jets (i.e. release velocity equal to or greater than local speed of sound) and the other three subsonic releases. The methane plume model in AltRAM matched both varieties well, with higher accuracy for the underexpanded releases.

For the jet flame model, we compared the heat flux and thermal radiation data reported from five separate turbulent jet flame experiments to the quantities calculated by AltRAM. Four of the five datasets were for underexpanded diffusion jets flames. While the results still match well enough to give a good estimate of what is occurring, the error is higher than what was seen with the plume model. For the underexpanded flames AltRAM provided reasonable approximations, which would lead to conservative risk assessments. Some modeling errors can be attributed to environmental effects (i.e. wind) since most large scale flame experiments are conducted outdoors.

AltRAM has been shown to be a reasonably accurate tool for calculating the concentration or flame properties of natural gas releases. Improvements could still be made for the plume of subsonic releases and radiative heat fluxes to reduce the conservative nature of these predictions. These models can provide valuable information for the risk assessment of natural gas infrastructure.

ACKNOWLEDGMENT

This research was supported by the office of Energy Efficiency and Renewable Energy's (EERE) Vehicle Technologies Office at the United States Department of Energy, under the Clean Cities subprogram. AltRAM owes its existence to the HyRAM software package (http://hyram.sandia.gov) and the authors gratefully acknowledge the developers and development of that package.

CONTENTS

LIST OF FIGURES

LIST OF TABLES

1. INTRODUCTION

The Alternative Fuels Risk Assessment Models (AltRAM) toolkit is an object-oriented Python module that enables the simulation of unignited dispersion, ignited turbulent diffusion flames, and indoor accumulation and delayed ignition of fuels. AltRAM currently supports different fluids including hydrogen, liquid hydrogen, methane (as a surrogate for compressed natural gas, or CNG) and liquid methane (as a surrogate for liquid natural gas, or LNG). This work is focused on the validation of the models for compressed natural gas (using methane as a surrogate). The validation only focuses on the unignited dispersion and turbulent flame models, not the indoor accumulation and delayed igntion models.

The objects in AltRAM relate to real-world, physical items and fluid properties. These Python objects can be assembled in various ways to describe a hydrogen release. Some of the Python objects have alternative underlying physics, or mathematical descriptions, so that different approaches can be compared. In this document, each of the Python objects within AltRAM are explained, and the compressed methane unignited dispersion models and flame models are compared to literature data.

2. ALTRAM DESCRIPTION

This report focuses on validating the unignited dispersion (jet) and flame models, and the description of AltRAM is limited to those specific models (and submodels). The models are based on work by Houf, Winters, Ekoto and others [1–4].

2.1. Model Components

2.1.1. Thermodynamics

AltRAM utilizes the CoolProp library [5], called through its Python interface to perform thermodynamic calculations. For methane, the property calculations are based on the work of Wetzmann and Wagner [6]. These thermodynamic calculations are used to calculate leak rates and are used in mass, momentum, and energy balances in regions close to the leak point. In other regions of the models, the ideal gas equation of state is used, as described in other sections.

2.1.2. Building the system

Three AltRAM objects (of two types) are needed to model an unignited dispersion (jet) or flame from CNG:

- Fluid objects are used in AltRAM to describe the compressed gas or liquefied gas in the case of LNG. These Fluid objects have attributes of a pressure, temperature, density (that are related through the CoolProp thermodynamics model), velocity, and species. The Fluid objects have methods to calculate the enthalpy, entropy, and other properties of the fluid. Fluid objects are also used to describe the ambient air.
- An Orifice object is simply a round hole through which the fluid object will pass. The Orifice object contains the attributes of a diameter (for a non-circular release, this needs to be an effective diameter), and a coefficient of discharge. An orifice objects has a method for calculating flow rates (discussed below in Section 2.1.3).

In order to simulate an unignited jet or a jet flame, the user needs to define a fuel Fluid object, an Orifice object, and an ambient Fluid object. Once these objects have been defined, the user can put these objects into a Jet or Flame object.

2.1.3. Engineering Zones

Both the AltRAM Jet and Flame objects require a fuel (fluid to be released), an orifice through which that fluid is being released, and an ambient object into which the fluid is being released. There are then several models and correlations that are used to simulate an unignited dispersion or flame. Both the flame and jet models begin with a developing flow region.

2.1.3.1. Orifice Flow

The first step is the flow through the orifice. An isentropic flow through the orifice is assumed, where:

$$s_0 = s_{\text{orifice}} \tag{1}$$

$$h_0 + \frac{v_0^2}{2} = h_{\text{orifice}} + \frac{v_{\text{orifice}}^2}{2} \tag{2}$$

where S is the entropy, h is the specific (on a mass basis) enthalpy, and v is the velocity. The model tries to find a solution where the flow is choked (v_0 is the speed of sound), although unchoked flows can also be defined and solutions can be found. If the flow is unchoked, it is recommended that the user also input the mass flow rate of the dispersion or flame model for improved accuracy.

2.1.3.2. Notional nozzle (underexpanded jet expansion)

If the flow is choked, then the pressure at the orifice will be higher than ambient pressure. An underexpanded jet notional nozzle model is used in this case to calculate the equivalent conditions of an atmospheric pressure flow rate and size that would give equivalent results. The user can specify several ways to model this section. In all cases, the mass flow through the notional nozzle remains constant, or

$$C_d \rho_{\text{orifice}} v_{\text{orifice}} \left(\frac{\pi}{4} d_{\text{orifice}}^2\right) = \rho_{\text{expanded}} v_{\text{expanded}} \left(\frac{\pi}{4} d_{\text{expanded}}^2\right) \tag{3}$$

where C_d is the coeficient of discharge, ρ is the density, and d is the diameter (or equivalent diameter if the release is non-circular).

In the default case, momentum is also conserved, or

$$\left(C_d^2 \rho_{\text{orifice}} v_{\text{orifice}}^2 + P_{\text{orifice}} - P_{\text{expanded}}\right)\left(\frac{\pi}{4} d_{\text{orifice}}^2\right) = \rho_{\text{expanded}} v_{\text{expanded}}^2 \left(\frac{\pi}{4} d_{\text{expanded}}^2\right) \tag{4}$$

where P is the pressure, and the pressure at the expanded plane is specified as being ambient. In the case where momentum is conserved, Eqs. 8 and 4 can be solved for the velocity at the expanded plane. If momentum is not conserved, the velocity at the expanded point is assumed to be sonic. Regardless of whether momentum is specified as being conserved, the temperature of the expanded fluid must also be specified, or energy conservation can be specified such that the temperature can be calculated. If energy conservation is specified (which is the default in the model), then the total enthalpy is conserved, similar to Eq. 2:

$$h_{\text{orifice}} + \frac{v_{\text{orifice}}^2}{2} = h_{\text{expanded}} + \frac{v_{\text{expanded}}^2}{2} \tag{5}$$

Alternatively, the temperature at the expanded plane can be assumed to be the temperature of the reservoir ('T0'), or if momentum is not conserved, the temperature of the reservoir or the temperature at the orifice ('Tthroat'). Since the pressure at the expansion plane is known (atmospheric), once the temperature at the expansion plane is specified or calculated and the velocity is known, the Fluid object at the expansion plane can be calculated.

These notional nozzle models are based off of several groups' works. Yüceil and Ötügen [7] describe the default AltRAM solution of solving the conservation of mass, momentum, and energy equations (Eqs. 8, 4, and 21). Birch et al. [8] solves the conservation of mass and momentum equations (Eqs. 8 and 4) but assume that the temperature at the expansion plane is the same as in the reservoir ('T0'). In earlier works, however, Birch et al. [9] assumed that the expansion plane fluid had a sonic velocity, the same temperature as the reservoir, and did not conserve momentum (only using Eq. 8). Ewan and Moodie [10] similarly do not conserve momentum, assume that the expansion plane velocity is sonic, but specify that the temperature of the fluid at the expansion plane is the same as the temperature at the throat (again, only using Eq. 8). Finally, Molkov et al. [11] conserves mass and energy between the throat and the expansion plane, but rather than conserving momentum, assumes that the fluid is sonic at the expansion plane (Eqs. 8 and 21).

2.1.3.3. Flow establishment

After flow through the orifice and/or the notional nozzle model, the flow is assumed to be a plug flow. Both the dispersion and flame models require the initial conditions of a Gaussian

distribution of concentration and velocity where

$$v = v_{\mathrm{CL}} \exp\left(-\frac{r^2}{B^2}\right) \tag{6}$$

$$\rho - \rho_{\mathrm{amb}} = (\rho_{\mathrm{CL}} - \rho_{amb}) \exp\left(-\frac{r^2}{(\lambda B)^2}\right) \tag{7}$$

$$\rho Y = \rho_{\mathrm{CL}} Y_{\mathrm{CL}} \exp\left(-\frac{r^2}{(\lambda B)^2}\right) \tag{8}$$

where B is the half-width of the jet and λ is the relative spreding ratio between the velocity and the scalar properties. The model for flow establishment describes the evolution from a plug flow to a Gaussian flow. Based on the work of Winters [12], the flow establishment length is $6.2d$ (note that in nearly all cases of gas flows, the densimetric discharge Froude number is $\geq \sqrt{40}$). The centerline velocity of the establishied, Gaussian flow is assumed to be the same as the plug flow

$$v_{\mathrm{CL,\ established}} = v_{\mathrm{plug}} \tag{9}$$

where the plug subscript denotes eitehr the expanded plane, or the orifice plane, if the orifice flow is subsonic. The jet half-width is found by simultaneously solving the continuity ($\rho v A = \text{constant}$) and momentum conservation equation ($\rho v^2 A = \text{constant}$), integrating the Gaussian profiles for the velocity (Eq. 6) and density (Eq. 7) to infinity at the established plane:

$$B_{\mathrm{established}} = \frac{d_{\mathrm{plug}}}{\sqrt{\frac{2(2\lambda^2+1)}{\lambda^2 \rho_{\mathrm{plug}}/\rho_{amb} + \lambda^2 + 1}}} \tag{10}$$

The enthalpy of the fluid is found, based on the mole fraction at the established plane, or

$$Y_{\mathrm{CL,\ established}} = Y_{\mathrm{plug}} \frac{\lambda^2 + 1}{2\lambda^2} \tag{11}$$

$$h_{\mathrm{CL,\ established}} = h_{amb} + \frac{\lambda^2 + 1}{2\lambda^2}(h_{\mathrm{plug}} - h_{amb}) \tag{12}$$

The heat capacity of the ambient air and hydrogen are estimated to be constant, and the density at the established plane is based on the centerline temperatre at the established plane, assuming an ideal gas equation of state or

$$c_{p,\mathrm{CL,\ established}} = Y_{\mathrm{CL,\ established}} c_{p,\ \mathrm{CH_4}} + (1 - Y_{\mathrm{CL,\ established}}) c_{p,\ amb} \tag{13}$$

$$T_{\mathrm{CL,\ established}} = \frac{h_{\mathrm{CL,\ established}}}{c_{p,\mathrm{CL,\ established}}} \tag{14}$$

$$MW_{\mathrm{CL,\ established}} = \frac{1}{Y_{\mathrm{CL,\ established}}/MW_{\mathrm{H_1}} + (1 - Y_{\mathrm{CL,\ established}})/MW_{amb})} \tag{15}$$

$$\rho_{\mathrm{CL,\ established}} = \frac{P_{amb} MW_{\mathrm{CL,\ established}}}{R T_{\mathrm{CL,\ established}}} \tag{16}$$

Once the flow has established into Gaussian profiles, either the unignited or flame models described below are used to calculate the propegation of those Gaussian profiles downstream.

2.2. Unignited dispersion modeling

Mass, species, momentum, and energy are conserved along the jet streamline to solve for the unignited propagation of the Gaussian profiles downstream. In other words:

$$\frac{d}{ds}\int_0^\infty \rho v 2\pi r dr = \rho_{amb} E \tag{17}$$

$$\frac{d}{ds}\int_0^\infty \rho Y v 2\pi r dr = 0 \tag{18}$$

$$\frac{d}{ds}\int_0^\infty \rho v^2 \cos(\theta) 2\pi r dr = 0 \tag{19}$$

$$\frac{d}{ds}\int_0^\infty \rho v^2 \sin(\theta) 2\pi r dr = \int_0^\infty (\rho_{amb} - \rho) g 2\pi r dr \tag{20}$$

$$\frac{d}{ds}\int_0^\infty \rho (h - h_{amb}) v 2\pi r dr = 0 \tag{21}$$

where s is the streamwise distance, $dx/ds = \cos(\theta)$, and $dy/ds = \sin(\theta)$, and E is the volumetric entrainement rate. The Gaussian profiles shown in Eqs. 6-8 can be substituted into these equations and the integrals can be evaluated, except for the case of energy conservation (Eq. 21), which can be numerically integrated, assuming that the enthalpy can be estimated as the product of a constant heat capacity and the temperature of the fluid (which is calculated using the ideal gas law). An explicit Runge-Kutta method of order (4)5 is used to integrate this system of equations downstream.

Entertainment is calculated as a sum of momentum and buoyancy contributions,

$$E = E_{mom} + E_{buoy} \tag{22}$$

where E_{mom} is a constant,

$$E_{mom} = \alpha_{mom} \sqrt{\frac{\pi/4 d^2_{\text{expanded}} \rho_{\text{expanded}} v_{\text{expanded}}}{\rho_{amb}}} \tag{23}$$

where $\alpha_{mom} = 0.282$, and E_{buoy} is based on the local Froude number

$$\text{Fr}_L = \frac{v^2_{\text{CL}} \rho_{\text{CL}}}{gB(\rho_{amb} - \rho_{\text{CL}})} \tag{24}$$

$$E_{buoy} = \frac{\alpha_{buoy}}{\text{Fr}_L} 2\pi v_{\text{CL}} B \sin(\theta) \tag{25}$$

where α_{buoy} is based on the global Froude number,

$$Fr = \frac{v_{\text{CL, established}}}{\sqrt{gB_{\text{established}}(\rho_{amb} - \rho_{\text{CL, established}})/\rho_{\text{CL, established}}}} \tag{26}$$

$$\alpha_{buoy} = \begin{cases} 17.313 - 0.11665\text{Fr} + (2.0771 \times 10^{-4})\text{Fr}^2 & \text{Fr} < 268 \\ 0.97 & \text{Fr} \geq 268 \end{cases} \tag{27}$$

2.3. Flame modeling

The flame model is the same as that described by Ekoto et al. [4]. Mass, momentum, and mixture fraction (rather than species mass) are conserved along the jet streamline to solve for the propagation of the Gaussian profiles downstream. In this case, the mixture fraction, or the mass fraction of the fuel stream in the system, is related to the mass fraction by

$$f = Y_{\mathrm{CH_4}} + Y_{\mathrm{H_2O}} \frac{MW_{\mathrm{CH_4}}}{MW_{\mathrm{H_2O}}} + Y_{\mathrm{CO_2}} \frac{MW_{\mathrm{CH_4}}}{MW_{\mathrm{CO_2}}} \tag{28}$$

The mixture fraction is assumed to have a Gaussian profile $f = f_{\mathrm{CL}} \exp[-r^2/(\lambda B)^2]$, and the conservation equations are:

$$\frac{d}{ds} \int_0^\infty \rho v 2\pi r dr = \rho_{amb} E \tag{29}$$

$$\frac{d}{ds} \int_0^\infty \rho f v 2\pi r dr = 0 \tag{30}$$

$$\frac{d}{ds} \int_0^\infty \rho v^2 \cos(\theta) 2\pi r dr = 0 \tag{31}$$

$$\frac{d}{ds} \int_0^\infty \rho v^2 \sin(\theta) 2\pi r dr = \int_0^\infty (\rho_{amb} - \rho) g 2\pi r dr \tag{32}$$

$$\tag{33}$$

In this case, the density does not have the radial profile given by Eq. 7, but is calculated based on the mixture fraction. The mixture is assumed to be thermally perfect, where the enthalpy of the products (which is a function of the temperature) is equal to the enthalpy of the reactants and the heat of combustion, or

$$\sum h_{\mathrm{products}}(T_{\mathrm{products}}) = \sum h_{\mathrm{reactants}}(T_{\mathrm{reactants}}) + \Delta H_c \tag{34}$$

The temperature of the products is iteratively found, and the density is calculated using the ideal gas equation. Once the density is known, Eqs. 29-32 are numerically integrated and an explicit Runge-Kutta method of order (4)5 due to Dormand & Prince is used to integrate this system of equations downstream.

Entrainment in the flame model has different parameters than the unignited dispersion model. Entrainment is still a sum of buoyancy and momentum contributions (Eq. 22), but the entrainment coefficient in the momentum equation (Eq. 23) has a different value, $\alpha_{mom} = 3.42 \times 10^{-2}$, and a numerically evaluated integral is used to calculate the buoyancy contribution

$$E_{buoy} = \frac{\alpha_{buoy} \sin(\theta) g}{B V_{\mathrm{CL}} \rho_{\mathrm{expanded}}} \int_0^\infty (\rho_{amb} - \rho) 2\pi r dr \tag{35}$$

and $\alpha_{buoy} = 5.75 \times 10^{-4}$.

3. DISPERSION OF SUBSONIC RELEASES

Gas releases with back pressures less than twice that of the surrounding environment yield small driving forces and produce subsonic jets. Thus, the escaping gas is released at the same pressure as the quiescent surrounding fluid. Jets of this nature are representative of small low-pressure leaks. Though leaks of this nature pose much lower risk in terms of property or occupant damage than higher backpressures, they are still of interest for model validation. Modeling results require the engineering zones for orific flow (Section 2.1.3.1) and Flow Establishment (Section 2.1.3.3), followed by the unignited dispersion model (Section 2.2).

3.1. Birch et al. (1984) [9]

In "The structure and concentration decay of high pressure jets of natural gas," Birch et al. [9] measured the concentration field in compressible sonic jets of natural gas with pressures from 2–70 bar using gas chromatography. Natural gas was released into quiescent air from an orifice with an internal diameter of 2.7 mm. For comparison, Birch et al. [9] also present the mean axial concentration of a subsonic natural gas jet. The subsonic release is discussed in this section, while the supersonic releases are discussed separately in Section 4.1.

3.1.1. Experimental Details

Birch et al. [9] do not give extensive details on the subsonic results in the the paper. We assume that the same apparatus (a 2.7 mm nozzle) and ambient conditions described in Section 4.1.1 was used at the lower reported back pressure of 1.14 bar_{abs}.

Due to the subsonic release conditions the average flow rate was approximated from the pressure differential through the short pipe equation. This could be a point of potential error since experimental flow rates were not reported.

3.1.2. Simulation Description

Similar to the simulations of Section 4.1.2 the model parameters are displayed in Table 3-1. Unlike the high-pressure simulations, a discharge coefficient of 0.8 was used. This is justified by the pressure dependency of discharge coefficient and the significantly reduced pressure in this release.

Due to modeling limitations, the release gas was assumed to be 100% methane, rather than the reported experimental gas which contained around 92% methane. Additionally, the ambient temperature and initial storage temperature of the gas was assumed to be 295 K since measured conditions were not reported.

Table 3-1 Simulation input parameters for experiments of Birch et al. [9].

Parameter	Value	Unit
Internal Diameter (d)	2.7	mm
Discharge Coefficient (C_d)	0.80	N/A
Ambient Pressure (Absolute)	1.01325	bar
Ambient Temperature (T_a)	295	K
Back Pressure (Absolute)	1.14	bar
Gas Initial Temperature (T_g)	295	K

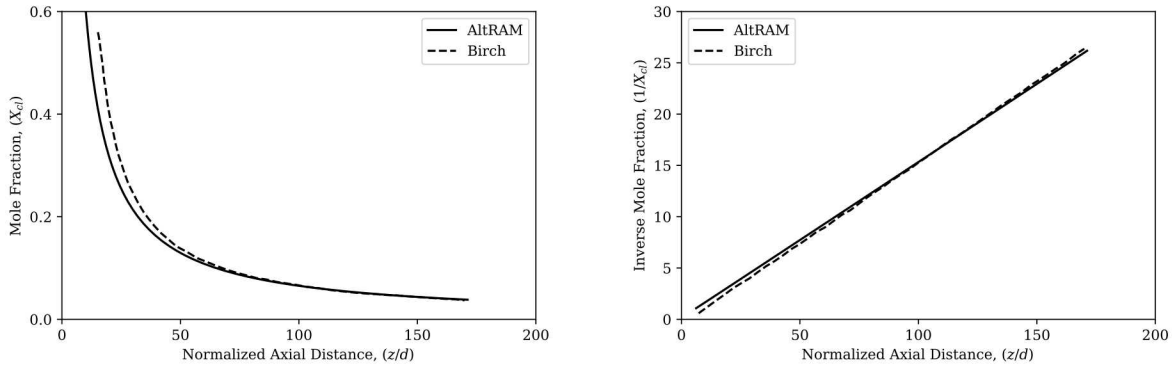

(a) Average axial mole fraction.

(b) Average inverse axial mole fraction.

Figure 3-1 Average centerline (a) mole fraction and (b) inverse mole fraction over normalized distance for subsonic release

3.1.3. Result Comparison

Experimental values of mean centerline concentration were presented. The inverse plot was also presented, along with curve fits to the experimental data. Figure 3-1 displays both the AltRAM simulated and experimental (curve fit) results.

AltRAM is in good agreement with the data, albeit slightly over-predicting the axial concentration decay. As mentioned earlier the flow rate for this subsonic release was obtained from the short pipe equation which is a potential source of error.

3.2. Richards and Pitts (1993) [13]

In “Global density effects on the self-preservation behavior of turbulent free jets,” Richard and Pitts carried out a series of experiments on jets to investigate if classical similarity relationships held, regardless of the source conditions3 [13]. The authors used Rayleigh light scattering in the

Table 3-2 Simulation input parameters for experiments of Richards and Pitts [13].

Parameter	Value	Unit
Internal Diameter (d)	6.35	mm
Discharge Coefficient (C_d)	1.0	N/A
Ambient Pressure (P_a)	1.01325	bar
Ambient Temperature (T_a)	295	K
Back Pressure (P_g)	1.01325	bar
Gas Initial Temperature (T_g)	295	K
Volumetric Flow Rate (Q)	2.083	Lit/s
Average Exit Velocity (v)	65.79	m/s

far-field to measure the concentration in two dimensions. In this section, we discuss a specific subsonic natural gas release.

3.2.1. Experimental Details

NG was released through a 6.35 mm orifice vertically into a quiescent environment of air at standard atmospheric conditions. No discharge coefficient was reported so a value of unity was assumed. The experimental gas used was 100% methane. Rayleigh light scattering diagnostics were used to obtain concentration measurements in the far field (10 to 60 orifice diameters).

3.2.2. Simulation Description

The flow rate was not directly measured but instead a Reynolds number (Re) of 25,000 was reported. From the Re and the reported assumption of fully developed turbulent pipe flow Q was approximated using Eq. 36. Table 3-2 displays all simulation parameters.

$$Q = \frac{\pi}{4} d \mathrm{Re} \mu \tag{36}$$

Note that due to a lack of reported experimental parameters the initial gas pressure and temperature were assumed ambient.

3.2.3. Result Comparison

The half-width (or distance from the axis where the mole fraction is half that at the axis) as a function of axial distance is shown in Figure 3-2. AltRAM slightly overpredicts the experimental half-width in the near-field (40 diameters downstream), matches well in the far-field (80

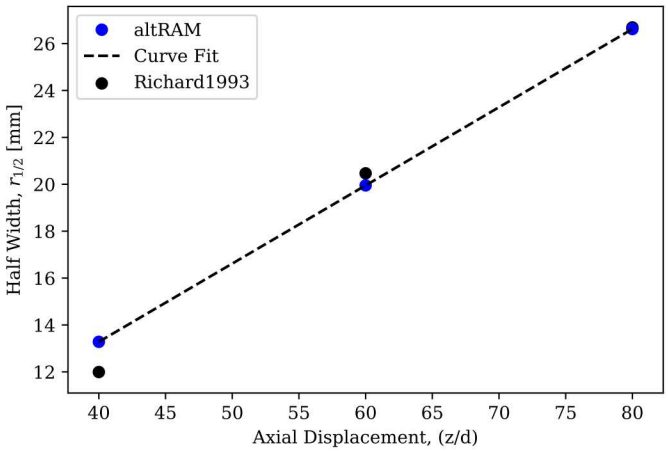

Figure 3-2 Concentration half-width over normalized distance

diameters downstream), and slightly under-predicts in between (at 60 diameters downstream). The overall trend agrees well with the experimental values and the predicted spread rate (slope) is linear, as expected from the literature on this subject. The simulated spread rate was $m_{sim} = 0.105$ which is less than the reported $m_{exp} = 0.115$ reported by Richards and Pitts. Richards and Pitts refer to the work of Chen & Rodi [14] and Fischer et al. [15] who report spread rates of $m_{exp} = 0.11$ and $m_{exp} = 0.106$. Therefore the spread rate computed from AltRAM falls within the values reported in the literature.

3.3. Birch et al. (1979) [16]

In "The Turbulent Concentration Field of a Methane Jet," Birch et al. [16] report on subsonic jets releases from large diameter tubes (approx. 0.5"). In this work, the authors used Raman scattering to measure the fluctuations in the turbulent jet concentration.

3.3.1. Experimental Details

The flow system consisted of a 12.65 mm tube with a length to diameter ratio of 50 and reported Reynolds number of 16,000. Birch describes the velocity profile being described well by the $1/7^{th}$ power law for turbulent pipe flow. The release gas was reported as approximately 95% methane.

Raman scattering of laser light was used to obtain concentration measurements of the expelling jet.

Table 3-3 Simulation input parameters for experiments of Birch et al. [16].

Parameter	Value	Unit
Internal Diameter (d)	12.65	mm
Discharge Coefficient (C_d)	1.0	N/A
Ambient Pressure (P_a)	1.01325	bar
Ambient Temperature (T_a)	295	K
Back Pressure (P_g)	1.01325	bar
Gas Initial Temperature (T_g)	295	K
Volumetric Flow Rate (Q)	2.656	l/s
Average Exit Velocity (v)	21.14	m/s

3.3.2. Simulation Description

No discharge coefficient was reported so a value of unity was assumed. Additionally, ambient conditions were not reported so standard atmospheric conditions were assigned. Since only Re was reported instead of mass flow rate or pressure differentials, the same techniques described in section 3.2.2 for obtaining mass flow rate were utilized. The reported and approximated simulated values used are displayed in Table 3-3.

Note the discharge coefficient, pressures, and temperatures were assumed unity and standard atmospheric conditions.

3.3.3. Result Comparison

Centerline concentration and inverse concentration were reported against normalized axial distance from the release point, shown in Fig. 3-3. The centerline concentration predicted by AltRAM is in good agreement with the reported experimental data, as can be seen in Fig. 3-3(a). The inverse concentration plot in Fig. 3-3(b) however, highlights differences in the concentrations in the far-field ($> 30d$).

Birch reported a near-field and far-field fit to show the variance in the decay constant (slope of the inverse concentration, k) computation. Birch et al. [16] differentiate the near- and far-field as 30 diameters from the release point. When linear fits to the near field data are extrapolated into the far field as shown in Fig. 3-3(c), the AltRAM predictions are in excellent agreement with the data. The dashed lines in Fig. 3-3(c) represent a linear fit to the modeled near field values, extrapolated into the far field. The same procedure was applied to the far field values, to find the corresponding decay rate. The resulting simulated decay constants are shown along with the experimental values in Table 3-4. The approximated errors between the two regions are vast. The discrepancies in the near and far field model accuracy has been attributed to the empirical entrainment model utilized by AltRAM, detailed in Section 2.2. Simulations (not shown here) showed that by increasing α_{buoy} by two orders of magnitude, the accuracy could be improved. Without further data for

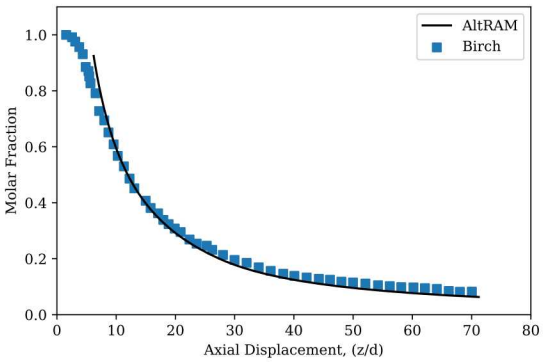

(a) Centerline molar concentration over normalized distance.

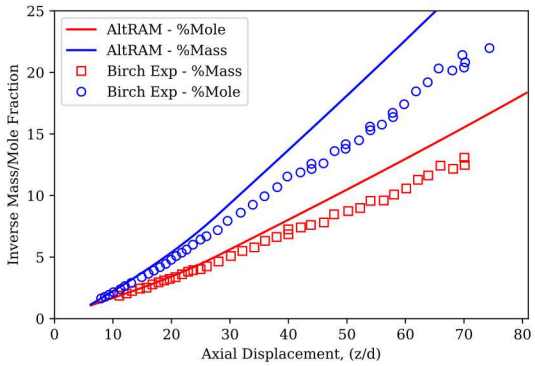

(b) Centerline inverse concentration over normalized distance.

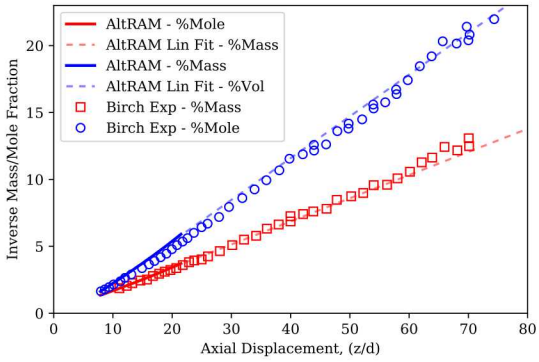

(c) Centerline inverse concentration over normalized distance. Simulations for the near-field ($10d \leq S \leq 30d$) extrapolated to the far-field.

Figure 3-3 Mole fraction and inverse mole fraction data from Birch et al. [16] compared to AltRAM simulations.

Table 3-4 Decay Constant Comparison.

Location	Modeled Decay Constant (k)	Experimental Decay Constant (k)	Error (%)
Near Field	4.31	4.7	8.3
Far Field	3.03	4.0	24.2

buoyancy dominated natural gas releases, however, the buoyancy constant in AltRAM has not been adjusted.

4. DISPERSION OF UNDEREXPANDED JETS

During a release through an orifice where the driving pressure exceeds approximately twice ambient, a choked flow is produced and the gas discharges as an underexpanded jet. An underexpanded jet can be described as a release where sonic flow conditions are witnessed at the throat and gas leaves the orifice at a higher pressure than that of the surrounding volume. Shocks occur in the region where the presure is reduced back down to ambient pressure. Jets of this nature (with a pressure at least twice that of ambient) are linked to the release from highly pressurized containers. Failure of NGV fuel tanks or the large pressurized tanks utilized in fueling stations are scenarios generally yield underexpanded jet releases.

4.1. Birch, et al. (1984) [9]

As described in Section 3.1, in "The structure and concentration decay of high pressure jets of natural gas," Birch et al. [9] measured the concentration field in compressible sonic jets of natural gas with pressures from 2–70 bar using gas chromatography. Natural gas was released into quiescent air from an orifice with an internal diameter of 2.7 mm. In this section, we discuss the high-pressure underexpanded jet releases.

4.1.1. Experimental Details

NG jets of back pressures ranging from 3.5-70 bar were released to quiescent air at standard conditions. The center line concentrations were recorded using rapid chromatograph in conjunction with a sampling nozzle. The release orifice had an internal diameter of 2.7 mm. The natural gas used for this work had methane content of 92-92.4% and a reported mean molecular weight of 17.32. Birch et al. [9] reported over all gas properties in Table 4-1. Birch commented

Table 4-1 Properties of experimental gas as reported by Birch et al. [9]

Gas	Molecular weight	ρ_g/ρ_a [†]	$\sqrt{\rho_g/\rho_a}$	γ	Sonic velocity at S.T.P. (m/s)	$\left(\frac{2}{\gamma+1}\right)^{\frac{\gamma+1}{2(\gamma-1)}}$
Natural Gas	17.32	0.5991	0.7740	1.35	421	0.582

[†]Relative density at 15°C and 1.013 bar, allowing for real gas behavior.

Table 4-2 Simulation input parameters for experiments of Birch, et al. [9].

Parameter	Value	Unit
Internal Diameter (ID)	2.7	mm
Discharge Coefficient (C_d)	0.85	N/A
Ambient Pressure (P_a)	1.01325	bar
Ambient Temperature (T_a)	295	K
Back Pressure (P_g)	3.5-70	bar
Gas Initial Temperature (T_g)	295	K

that a discharge coefficient $C_d = 0.8$ was appropriate for subsonic conditions but as back pressure increases so does C_d [9]. Due to the uncertainty in this parameter, it was varied slightly in the AltRAM simulations, with $C_d = 0.85$ found to yield a better match to the experimental results.

4.1.2. Simulation Description

Matching the reported parameters, the diameter of the simulated nozzle was set to 2.7 mm with a discharge coefficient of $C_d = 0.85$. Ambient conditions were not explicitly defined and therefor were assumed to be as shown in Tab. 4-2.

4.1.3. Result Comparison

Birch reported inverse centerline concentration against normalized downstream distance for all underexpanded jet releases. The distance was normalized by the orifice internal diameter and scaled by the square root of the pressure ratio between storage and ambient for each release. Experimental data was extracted for two cases, one for only the 3.5 bar release, and the other which contained the full experimental range. The extracted results are compared to those produced by AltRAM in Fig. 4-1.

For clarification the dashed line in Fig. 4-1(a) is not the same as that in Fig. 4-1(b). For Fig. 4-1(b) the dashed line represents a linear fit to all experimental data whereas Fig. 4-1(a) is a fit to only the 3.5 bar release (the normalization along the x-axis is also different in these two plots). As seen AltRAM nearly generates the experimenally observed self-similar collapse over the simulated pressure range and the simulated results are in good agreement with the experimental data. The cumulative concentration decay rate (slope of the line) obtained from AltRAM equated to $k = 4.52$ which agrees well with the reported experimental value of $k = 4.45$.

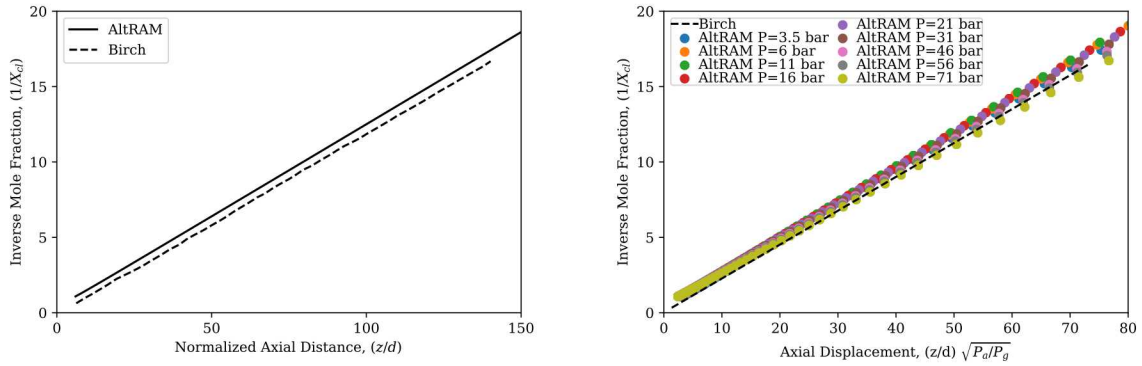

(a) Inverse mean centerline axial concentation decay for the 3.5 bar NG release.

(b) Experimental fit and simulations of axial concentration decay for the 3.5-70 bar NG release.

Figure 4-1 Inverse mole fraction as a function of normalized axial distance. Note there is a difference in the x-axis scales between the two plots.

4.2. Birch et al. (1988) [17]

In "Flame Stability in Underexpanded Natural Gas Jets," Birch et al. [17] study the flame stability as a function of the orifice diameter. Although this paper discusses large natural gas jet flames, there are some reported concentrations that are compared to our unignited dispersion model in this section.

4.2.1. Experimental Details

In this experiment large scale NG jets were ignited in order to obtain a stable light-up distance. Various underexpanded jets were released from orifice diameters ranging from 19-35 mm. Reported pressure ratio of the back pressure over ambient can be seen in Table 4-3. From these conditions Birch computed the centerline mean concentration at specific axial locations using Eq. 37 given by Brennan et al. [18]:

$$X_{\mathrm{CL}} = \frac{kd}{S+a}\sqrt{\frac{\rho_a}{\rho_g}} \tag{37}$$

Where k d, S, and a, represent the concentration decay constant, internal nozzle diameter, downstream distance from release, and virtual origin, respectively. Densities are denoted by ρ with the subscripts a and g denoting ambient and natural gas, respectively. Also note that $\rho_a/\rho_g \propto P_a/P_g$ for ideal gas behavior.

From this single report a wide variety of jets were available for model validation. As mentioned the reported concentration data was obtained from the empirical relation described by Eq. 37. This equation was used to approximate the centerline concentrations at the downstream light up distances.

Table 4-3 Jet Release experiment parameters

Nozzle diameter [mm]	Stagnation Pressure P/P_a	Light-up distance [m]	Concentration [%-volume]
19	22.42	5.17	8.57
19	22.57	5.67	7.82
25	15.25	5.43	8.89
25	15.25	6.27	7.70
35	17.20	8.79	8.22
35	17.28	8.82	8.18
35	17.34	8.31	8.69
35	30.60	11.57	8.21

Table 4-4 Simulation input parameters for experiments of Birch et al. [17]

Parameter	Value	Unit
Internal Diameter (d)	19, 25, 35	mm
Discharge Coefficient (C_d)	1.0	N/A
Ambient Pressure (P_a)	1.01325	bar
Ambient Temperature (T_a)	295	K
Back Pressure (P_g)	15.45 - 31.00	bar
Gas Initial Temperature (T_g)	295	K

4.2.2. Simulation Description

Utilizing the reported nozzle diameters and pressure ratios multiple simulations were run. The discharge coefficient was not reported so an assumption of unity was taken. It has been shown in multiple studies that the discharge coefficient increases with pressure ratio (e.g., see [9, 19]). Thus, the assumption of C_d equal to unity is not unreasonable. Table 4-4 displays the overall input deck for AltRAM simulation. The ambient conditions as well as the initial gas reservoir temperature was not reported and assumed to be standard atmospheric conditions.

4.2.3. Result Comparison

Since the main purpose of the Birch et al. paper [17] was to analyze the stable light up distance of underexpanded NG jets, centerline concentrations were only reported at the determined light up distances. Figure 4-2 shows the reported empirical concentration values obtained from the experimental data compared to those simulated by AltRAM. AltRAM is consistently underpredicting the concentration relative to the reported values, but it should be noted that the

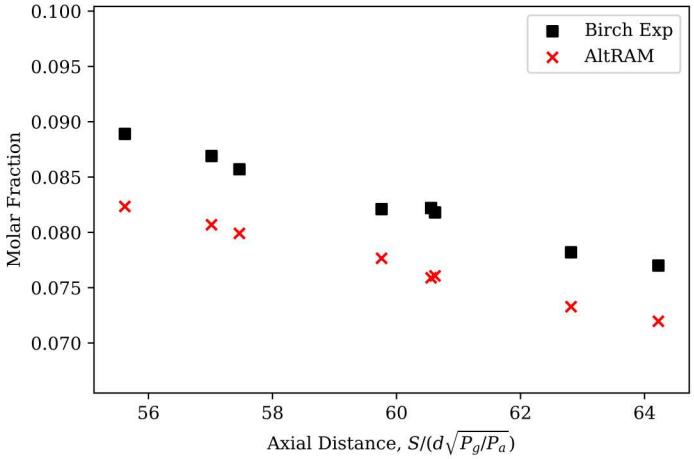

Figure 4-2 Molar concentration versus effective light up distance normalized by effective diameter

concentrations in this case were calculated by an empirical formula rather than being experimentally measured. It is possible that the empirical values in the formula are systematically off. The maximum error witnessed was 7.46%, showing that the AltRAM simulations are in relatively good agreement with the empirical formulas of Brennan for a range of cases.

4.3. Brennan et al. (1984) [18]

In "Dispersion of High Pressure Jets of Natural Gas in the Atmosphere," Brennan et al. [18] extended the underexpanded jet study from Birch et al. [9]. The scope of this study was to extend Birch's work on high pressure small scale jets into larger scale releases to determine the effect of pressure and atmospheric conditions on the jet behavior. Due to the scale of the jets and scope of the study all experiments were conducted outdoors.

4.3.1. Experimental Details

The experimental setup included nozzle orifice of 25, 50, and 76 mm and pressures ranging from 5-57 bar absolute. The recorded wind speeds ranged from 1 to 11 m/s. The scaling factors used to normalize the streamwise distance was pseudo-diameter (or effective diameter as defined by others). According to Brennan, the pseudo-diameter (d_{ps}) is computed as shown in Eq. 38 and is representative of a diameter which yields the same mass flow rate as the underexpanded release with a uniform velocity profile of $\vec{v} = c$ where c is the speed of sound of the released gas.

$$d_{ps} = d\sqrt{0.582 C_d P_g / P_a} \tag{38}$$

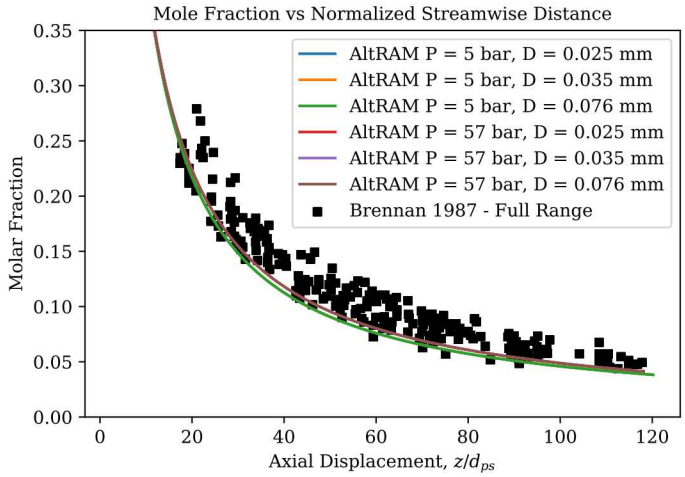

Figure 4-3 Centerline concentration vs normalized distance for large scale jets. Data is from Brennan et al. [18]. Due to the scaling, the AltRAM lines collapse under the green and brown lines.

Where C_d represents the discharge coefficient which was taken as 0.85. Pseudo-diameters were calculated for each experimental configuration and used as a scaling parameter for the results.

4.3.2. Simulation Description

All mentioned internal diameters were utilized to generate the simulated results. For pressure the highest and lowest reported values were used to obtain a range of results from the models. Ambient conditions as well as initial stored gas temperatures were assumed to be that of standard atmospheric conditions. The simulated downstream distance matched that of the experimental measurements.

4.3.3. Result Comparison

Brennan et al. [18] displayed centerline concentration values versus normalized distance of all experiments on one plot. The obtained values from the max and min pressures at all diameters are shown with the experimental data in Fig. 4-3.

Even though multiple simulations were ran, since the results were scaled by the pseudo diameters, the diameter variant simulations nearly collapse onto a single curve. It can be seen that the predicted concentration contour in the streamwise direction matches with the lower end of the experimental profile. Differences in results may be attributed to experimental uncertainty or atmospheric effects not considered by the models within AltRAM.

Table 4-5 Experimental Parameters

Release Configuration No	Release Direction In Relation To Wind Direction	Release Orifice	Pipe Bottom Height Above Gnd. [m]	Nominal Plenum Chamber Pressure bar	Nominal Gas Release Rate [kg/s]
1	Horizontal - downwind	Hole	4.5	20	18-19
2	Horizontal - upwind	Hole	4.5	20	18-19
3	45° above horizontal–downwind ("low" wind)	Hole	0.75	20	18-19
4	45° above horizontal–downwind ("high" wind)	Hole	0.75	20	18-19
5	Vertically upward	Hole	0.75	20	18-19
6	Vertically upward	Hole	0.75	70	60-64
7	Vertically upward–wind normal to pipe axis	Slot	0.75	20	18-19
8	Vertically upward–wind parallel to pipe axis	Slot	0.75	20	18-19
9	Vertically downward	Hole	0.75	70	60-64
10	45° below horizontal–downwind	Hole	0.75	70	60-64
11	Horizontal–downwind	Hole	0.75	70	60-64
12	Horizontal–downwind	Hole	0	70	60-64

Brennen reported a decay constant of $k = 5.08$ where the decay constant was obtained from equation 37. When k was computed using the min pressure data set for $P_g = 5$ bar, a value of $k = 4.69$ was obtained. Whereas the $P_g = 57$ bar data set yielded $k = 5.08$.

4.4. Hankinson et al. (2000) [19]

In “Experimental Studies of Releases of High Pressure Natural Gas from Punctures and Rips in Above-Ground Pipework,” Hankinson et al. [19] investigate the dispersion and combustion outcomes of releases from above ground high pressure pipelines. The unignited dispersion results are discussed here while the combustion results are duscussed in Section 6.2.

4.4.1. Experimental Details

Natural gas was stored at 20 bar and released through an orifice of 75 mm. Between experimental releases the orifice surface normal (or jet streamwise direction) was varied. All experimental configurations are shown in Table 4-5.

Experimental values were only reported for experimental configuration 1 and 4. Note that for configuration 4 the wind was referred to as high. The wind speed ranged from 7.2 to 8.0 m/s.

A detailed image of the experimental release pipe is shown below in Fig. 4-4. The gas supply line connected to a 1.5 m plenum chamber which was pressurized and maintained at 20 bar during release. The 75 mm hole was located at the center of the plenum chamber and was oriented in direction as described in Table 4-5. Concentration values of the release jet were captured utilizing

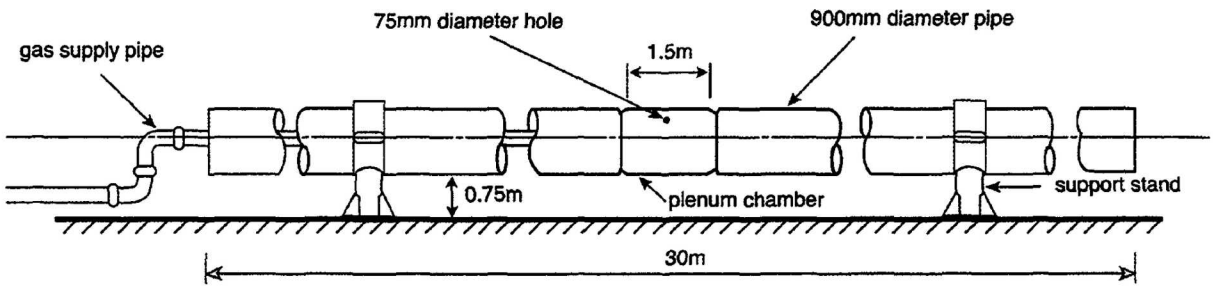

Figure 4-4 Schematic of experimental arrangement (hole position representative of configuration 4 [19].

a Raman LIDAR system, see full report for details [19].

4.4.2. Simulation Description

As mentioned only configuration 1 and 4 were used for validation. Therefore, highlighted parameters in Table 4-5 were used to construct the model. The release orifice column refers to the orifice as a "hole". It was not explicitly stated if this hole is located on a mounted orifice plate or drilled directly into the (curved) 900 mm pipe. A geometric evaluation showed that only a 0.1% cross-sectional area difference results between the two options, so 75 mm was used in the simulations. Additionally, a discharge coefficient for the supply line was reported but not for the release orifice, thus $C_d = 0.9$ was used since this value was reported in similar work carried out by Lowesmith and Hankinson [20].

4.4.3. Result Comparison

Concentration levels for 5% and 2.5% by volume were reported for both configurations. Figure 4-5 shows both configurations, where the black lines represent the experimental 5% concentration contour and the black "x" marks represent the 2.5% contours. The black dashed lines represent the author's approximate 5% contour, which are not from measurement. Presented on top of the experimental results, the colored contour plot along with the two white lines represent the concentrations obtained from AltRAM. The two white lines also correspond to the 5% and 2.5% concentration profiles. In both configurations wind may have attributed to inconsistencies between concentration profiles. For the horizontal configuration (Fig. 4-5(a)), even though wind is in the same direction as the release, turbulent effects can increase mixing which is known to increase the rate of diffusion. The wind effect is more apparent for the 45° release (Fig 4-5(b)), where the wind convects the jet downwind of its initial trajectory (in the x-direction).

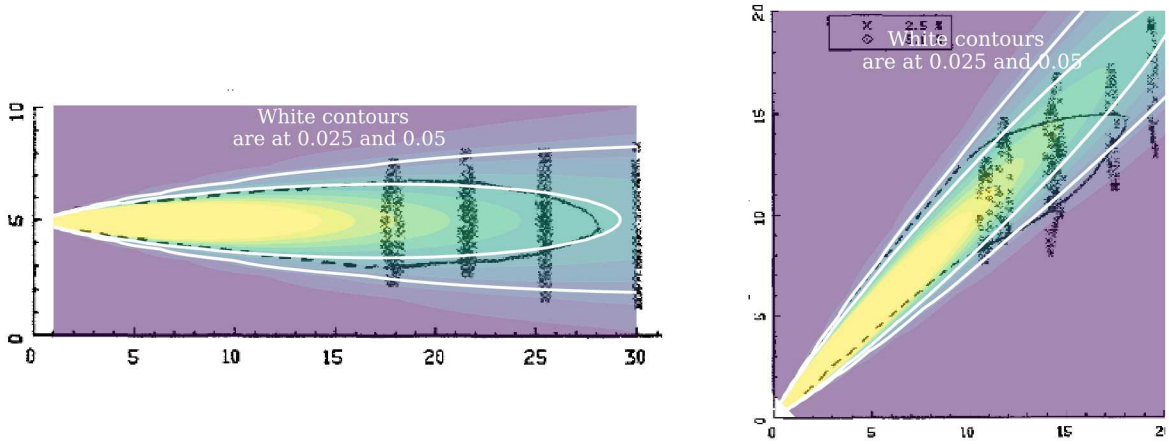

(a) Horizontal release. **(b)** 45° release

Figure 4-5 Concentration contours (AltRAM – Colored Contours and white lines, Experimental – Black lines and 'x' markers).

In the momentum dominant regions where wind makes up a small percentage of the total driving forces, experimental and modeled trajectory and concentration are in good agreement.

5. SUBSONIC JET FLAMES

As explained in Section 3, gas releases with low back pressures will yield subsonic jets. Ignition of these low momentum jets will typically yield buoyancy dominated flames. In the following section, the jet flame models contained within AltRAM are evaluated for this special case.

5.1. Baillie et al. (1998) [21]

In "A phenomenological model for predicting the thermal loading to a cylindrical vessel impacted by high pressure natural gas jet fires," Baillie et al. [21] produced subsonic small scale jet flames in a laboratory setting in order to validate an independently developed radiation model. The radiative heat flux measurements were reported at specified locations within the quiescent test space.

Table 5-1 Simulation input parameters for experiments of Baillie et al. [21]

Parameter	Value	Unit
Discharge Coefficient (C_d)	1	N/A
Ambient Pressure (P_a)	1	bar
Ambient Temperature (T_a)	295	K
Initial Gas Temperature (T_g)	295	K
Internal Diameter (d)	8.6	mm
Initial Gas Pressure (P_g)	N/A – Assumed 1	bar
Average Exit Velocity ($\vec{v}$)	20	m/s
Release Angle (θ)	90	deg
Relative Humidity (RH)	N/A Assumed 1	-
Radiometer Height (h_r)	0	m

5.1.1. Experimental Details

Methane at a concentration of (99.99%) was released from 8.6 mm (ID) vertical pipe. A second concentric pipe of 23 mm provided a small co-flow of air through the annular channel to provide rim-stabilization for the flame. The luminous flame height was reported as 1.1-1.2 m tall. During the duration of the jet flame, a radiometer was displaced vertically (parallel to the flame trajectory) to form heat flux profiles. The same technique was repeated in the horizontal direction (perpendicular to the flame trajectory). For the horizontal profile the height of the radiometer was at the release point. For the vertical displacement the radiometer was offset from the jet center line by 0.4 m.

5.1.2. Simulation Description

The simulation parameters are shown in Table 5-1. The discharge coefficient was assumed to be 1.

5.1.3. Result Comparison

As mentioned radiation measurements were obtained by tracking a radiometer vertically and horizontally. Heat flux values from equivalent spatial locations were extracted from AltRAM. Comparison between the experimental and modeled results are shown in Figure 5-1(b)

Both vertical and horizontal heat flux magnitudes were over-predicted by AltRAM. For profile shape the axial (or perpendicular) shape agreed well with the experimental data. The simulated vertical profile produced a shifted Gaussian profile with lesser slopes. The disagreement on steepness could be attributed to the co-flowed air which could increase the rate of combustion and was not accounted for by the model. The heat flux values were over-predicted but not outside of the range of reasonable values. Also note the modeled values would lead to more conservative choices with respect to safety and design.

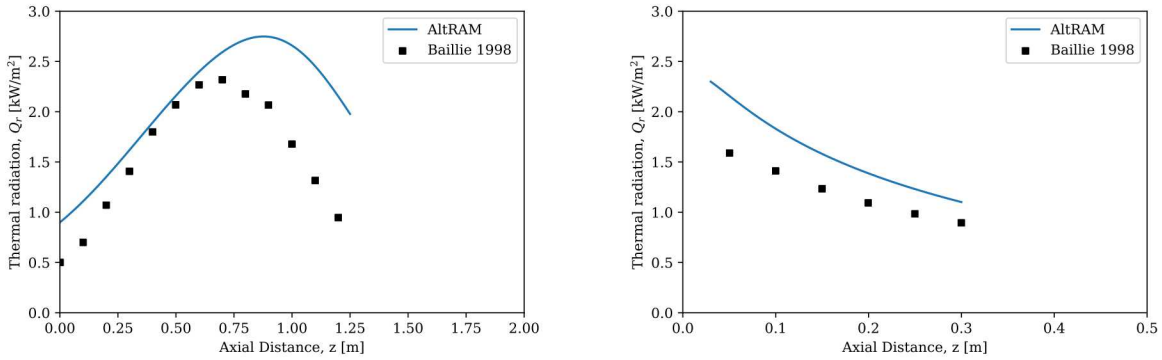

(a) Vertical measurements.

(b) Axial measurements.

Figure 5-1 Thermal radiation as a function of vertical and axial displacement. Baillie 1998 refers to Baillie et al. [21].

6. UNDEREXPANDED JET FLAMES

As explained in Section 4, with large enough pressure gradients, gas releases can produce underexpanded jets. The ignition of these high momentum jets can induce large scale flames. Whether released vertically or horizontally with respect to the ground, buoyancy plays a large role due to the drastic density ratios of the hot combustion products to that of the surrounding ambient air. Within this section large scale experiments are replicated using the AltRAM models.

6.1. Lowesmith and Hankinson (2012) [20]

In "Large scale high pressure jet fires involving natural gas and natural gas/hydrogen mixtures," Lowesmith and Hankinson [20] discribe six large scale high pressure jet flame experiments, three of which utilized natural gas. Due to the scale of the releases, the tests were carried out in the outdoor facilities of the GL Noble Denton Spadeadam Test Site located in Cumbria, UK. The purpose of the test was to measure the heat transfer from large-scale flames when impinged upon an object.

6.1.1. Experimental Details

The impinged object in this case was a pipe located at the approximate half length of the flame. A series of radiometers were located perpendicular to the flame trajectory at the downstream distance of the pipe or 5 m beyond. The pipe and radiometer locations were variable since they were moved to half the flame length of the various releases. A representation of a "typical" test configuration is shown in Fig. 6-1.

As shown, in the downwind direction, the first row of radiometers were located in close proximity to the instrumented pipe. The second row of radiometers were placed further downwind. The

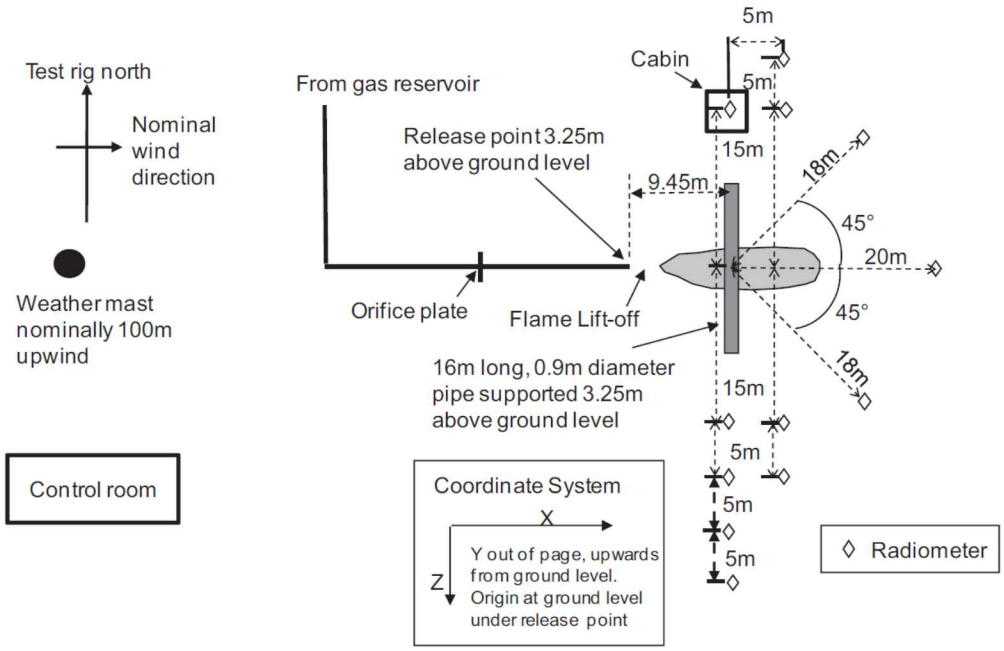

Figure 6-1 Test configuration for a representative setup (locations of pipe and sensors varied) [20]

Table 6-1 Test conditions and release parameters [20].

Test Number	Release Diameter [mm]	Gauge Pressure [bar]	Pipe Distance [m]	Wind Direction [deg]	Wind Speed [m/s]
1	20	59.4	9.45	1 ± 11 S	6.3 ± 1.5
2	35	61.5	15.45	27 ± 5 S	6.2 ± 0.5
3	50	58.8	21.61	3 ± 13 N	3.6 ± 0.5

exact downwind locations were extracted from the report. Additionally Lowesmith reported the radiometer used had an accuracy of $\pm 5\%$.

As shown in Fig. 6-1, wind measurements were taken 100 m upwind of the release point. The measured wind and key experimental parameters are listed in Table 6-1 for all three NG releases. Note the wind directions reported in Table 6-1 are deviation from the release direction (east) and the release point was located 3.25 m off the ground.

6.1.2. Simulation Description

Experimental radiative heat flux measurements were modeled in AltRAM utilizing the experimental parameters reported in Table 6-1. Table 6-2 summarizes the models initializing parameters.

Table 6-2 Simulated input parameters for experiments of Lowesmith and Hankinson [20]

Parameter	Test 1	Test 2	Test 3	Unit
Internal Diameter (d)	20.0	35.0	50.0	mm
Discharge Coefficient (C_d)	0.9	0.9	0.9	N/A
Ambient Temperature (T_a)	278	278	278	K
Ambient Pressure (P_a)	1.0	1.0	1.0	bar
Gas Storage Temperature (T_g)	281	281	281	K
Gas Storage Pressure (P_g)	59.4	61.5	58.8	bar

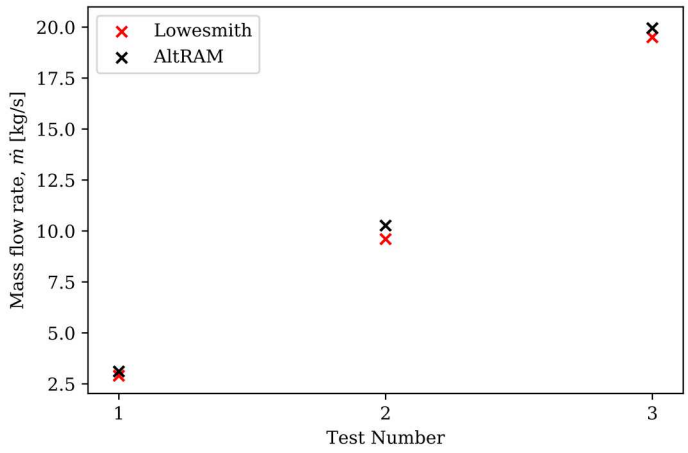

Figure 6-2 Simulated and measured mass flow rate per test configuration

Assumptions and potential sources of error include the experimental gas composition, the height of the radiometers, and the current unaccounted effects of wind. For the gas composition a methane concentration of 93% was reported. AltRAM only models pure concentrations currently thus the simulation assumes the gas to be pure methane. For the radiometer location, Lowesmith did not report the height, thus the height was varied in the simulations from ground level up to jet flames release point centerline height. In terms of ambient conditions, relative humidity was not listed and assumed a value of unity.

6.1.3. Result Comparison

Due to the large pressure gradients all releases were underexpanded jets as described in Section 4. Under these conditions the mass flow rate is computed assuming a choked flow within AltRAM. The computed mass flow rates are compared to the reported experimental values in Fig. 6-2. The simulated values are in good agreement with the values reported by Lowesmith. The approximate error between each test is shown in Table 6-3. The experimental mass flow rates were obtained from pressure and temperature measurements across the orifice plate. The accuracy of the

Table 6-3 Mass flow rate comparison

Test Number	Measured $\dot{m}$ [kg/s]	Modeled $\dot{m}$ [kg/s]	Error [%]
1	2.9	3.22	11.27
2	9.6	10.26	6.91
3	19.5	19.94	2.29

pressure sensors was reported as $\pm 0.15\%$ with a response time of 0.3 s. The temperature was gathered with a type T thermocouple connected to a transmitter with a reported accuracy of $\pm 0.5^{\circ}$C. Factoring in experimental uncertainty the model predictions of mass flowrate are within reasonable range of the measured values.

Temperature contour plots of all three releases were generated, as shown in Fig. 6-3. This provides a visual comparison of the simulated flame trajectory against the experimental images shown in Figs. 6-3(a), 6-3(c), and 6-3(e) vs. Figs. 6-3(b), 6-3(d), and 6-3(f). The temperature contours show the flame is rising upwards due to buoyancy as it travels away from the release point downstream. Unlike the experimental images, the simulated flames never impinge directly onto the pipe. This could be due to over-prediction of buoyancy or from unmodeled effects caused by wind.

In terms of radiative heat flux, the measured values were divided into two groups. Radiometers that were located north of the initial flame trajectory and those located south. The cross-flow effects of wind can be seen in the results displayed in Figs. 6-4(a) and 6-4(b).

For the same tests, at equivalent radial distances, southern located radiometers reported higher heat flux values than northern equivalents. We speculate that this is due to the convective effects wind had on the flame trajectory. Furthermore, it can be observed that the measured differences between radially equivalent northern and southern locations were largest for tests 1 and 2 which had the highest reported wind speeds.

The simulated values over-predict the experimental results even when the radiometers are assumed to be at ground level. This problem is exacerbated in the northern locations for reasons explained above. Overall the simulated results over-predict the values reported from experiment by 2-8 kW/m^2.

6.2. Hankinson et al. (2000) [19]

In "Experimental Studies of Releases of High Pressure Natural Gas from Punctures and Rips in Above-Ground Pipework," Hankinson et al. [19] report on flames and unignited dispersion of natural gas from simulated punctures and rips in natural gas transmission lines. In addition to the concentration contours reviewed in Section 4.4, Hankinson et al. [19] reported radiative heat flux measurements for jet flames produced from configurations 1 and 4 listed in Table 4-5. For full experimental description see Section 4.4.

(a) Snapshot of experimental flame, test 1 [20].

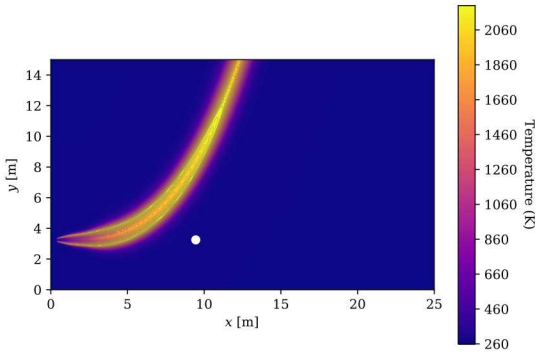

(b) Temperature contour plots, test 1.

(c) Snapshot of experimental flame, test 2 [20].

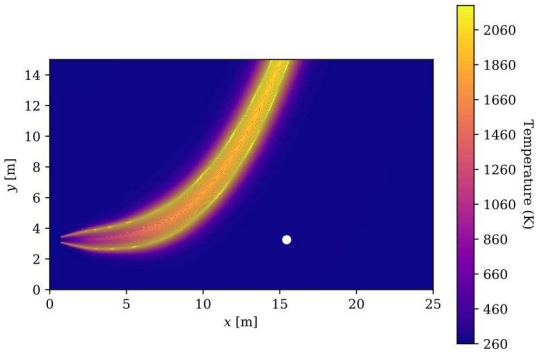

(d) Temperature contour plots, test 2.

(e) Snapshot of experimental flame, test 3 [20].

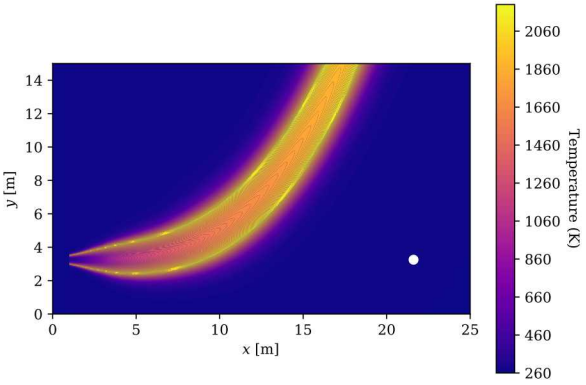

(f) Temperature contour plots, test 3.

Figure 6-3 Experimental and simulated trajectories of flames. Note that the images are not at the same scale, and may not be the same scale as the simulations. The white 'o' in the simulations represents the pipe.

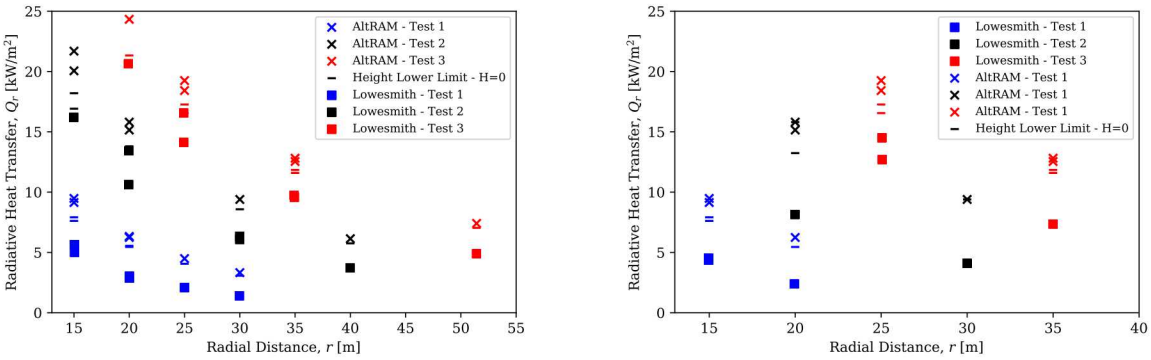

(a) Measurements south of flame trajectory.

(b) Measurements north of flame trajectory.

Figure 6-4 Incident radiation measured in two directions from the release point. Lowesmith label refers to Lowesmith et al. [20].

6.2.1. Experimental Details

As mentioned experimental setup for the jet flames was the same as that described in Section 4.4.1. Relative humidity was reported as 0.89 and the radiometer locations were oriented to obtain spatial radiation profiles. Average wind speed measured 10 m above the ground were reported as 7.4 m/s and 8.2 m/s for the horizontal and 45° release. It was determined from experimental observations that the wind was blowing in the same direction as the horizontal release.

6.2.2. Simulation Description

The reader is referred to Section 4.4.2 for simulation description details.

6.2.3. Result Comparison

The incident radiation per release was measured across an array of radiometers located downwind, crosswind, and upwind of the release point. The experimental thermal radiation profiles are compared to those obtained from AltRAM in Fig. 6-5.

Similar to the results in Section 6.1.3, the simulated results over-predict the majority of the thermal radiation profiles especially for the upwind locations. Additionally, thermal radiation gradients are steeper in the experimental results for the downwind profiles of both releases and the crosswind profile of the horizontal release. This could be attributed to turbulent and convective effects from wind. This seems likely especially when comparing upwind profiles. Hankison et al. [19] describes observation of the wind pulling the flame in the downwind direction. This

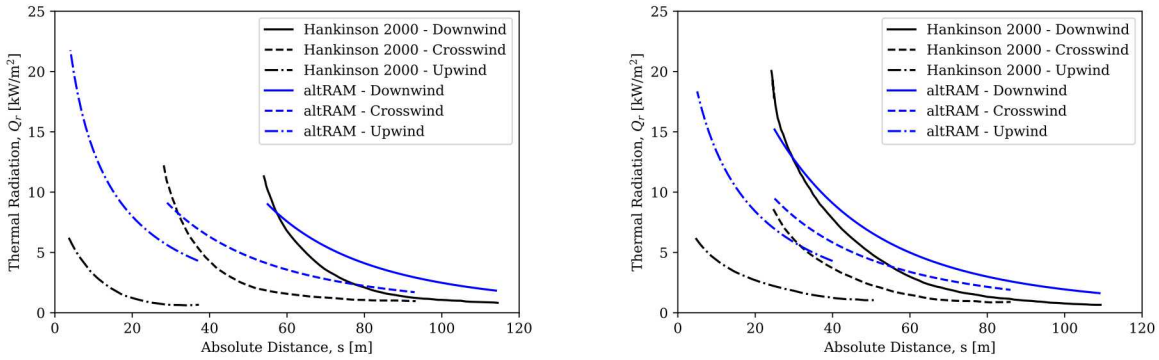

(a) Horizontal release.

(b) 45° release.

Figure 6-5 Radiation profiles for down/cross/up wind locations. Hankinson 2000 refers to Hankinson et al. [19]

would lead to a significant reduction in radiative heat transfer in the upwind direction and provide some insight as to why values produced by AltRAM exceed the reported experimental results.

Hankison et al. [19] also reported the maximum horizontal distance for thermal radiation levels of 5 kW/m^2 for both releases. These values were obtained from AltRAM utilizing heat flux contour plots. The contour plots for heat flux are shown in Fig 6-6. Hankison reported horizontal distances of 64 m and 48 m for the horizontal and angled 45° release. The contour plots yielded maximum horizontal distances of 81 m and 73 m. This aligns with the previous results shown in Fig. 6-5where the radiative heat flux is over-predicted.

6.3. Lowesmith and Hankinson (2013) [22].

In "Large scale experiments to study fires following the rupture of high pressure pipelines conveying natural gas and natural gas/hydrogen mixtures," Lowesmith an Hankinson [22] filled a 150 mm diameter section of pipeline connected to a 300 mm diameter reservoir with NG pressurized to 70 bar. The 150 mm section of pipe was ruptured, and the released gas was ignited. Initially a large fireball formed proceeded by a large burning jet flame which was sustained by the outflow gas of the reservoir. The purpose of the experiment was to understand the associated risks and hazards of an ignited ruptured pipeline.

6.3.1. Experimental Details

The gas filled 150 mm section of pipe was ruptured and the vertically released gas was ignited. The ignition source was an incendiary charge which was activated immediately after pipe rupture. The pipe was ruptured in such a way that the outflow escaped through the full bore of the pipe. The mass flow rates of the pipe was determined by pressure and temperature measurements made at an orifice plate located between the ruptured pipe and 300 mm reservoir. Radiometers were

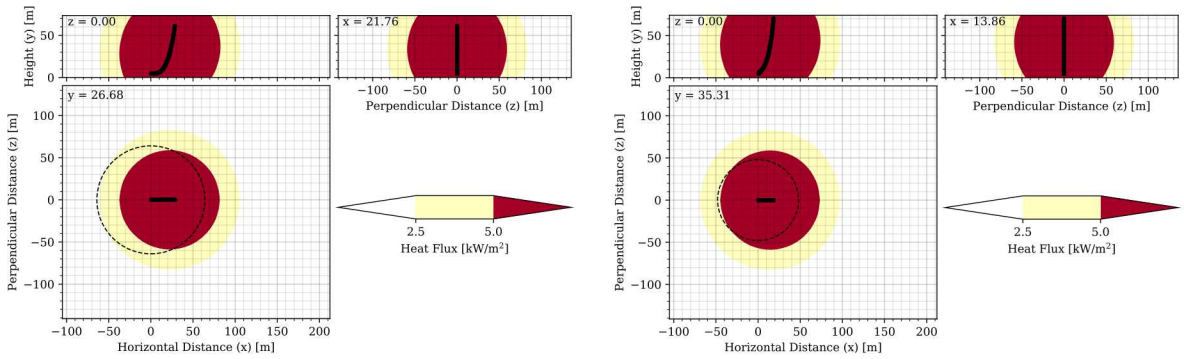

(a) Horizontal release.

(b) 45° release.

Figure 6-6 Radiative heat flux contours for the simulated horizontal and 45° releases. The dashed circle are the 5 kW/m^2 heat flux contours reported by Hankinson et al. [19].

Table 6-4 Wind conditions.

Height [m]	Speed [m/s]
2.9	4.8 ± 1.0
4.7	5.1 ± 1.0
8.4	5.6 ± 1.1
10.9	5.7 ± 1.4

utilized to capture heat flux values at various locations multiple times over the course of the combustion. The radiometers were reported to have a response time of 1 second and accuracy of $\pm 5\%$. Fig. 6-7 shows the radiometer locations with respect to the release point. As shown, the radiometers were located perpendicular the flames vertical trajectory, this direction will be referred to as radially going forward. The radial positions ranged from north east to south west. Also note that Fig. 6-7 displays the wind direction for test 2, where test 2 correlates to the NG release. Wind was measured at various heights to capture a more complete velocity profile. The wind speeds and their corresponding heights are shown in Table 6-4.

6.3.2. Simulation Description

As mentioned in Section 6.3.1, rupture of the pipe yielded an outflow diameter of 150 mm. The release trajectory was vertical from the ground and no discharge coefficient was reported thus a value of unity was assumed. Table 6-5 displays all the experimental parameters used as inputs to the simulation.

In addition to the experimental parameters and initial conditions Lowesmith et al. [22] also provided the total measured mass flow versus time. Utilizing the parameters listed in Table 6-5 and the transient mass flow data, the pressure time profiles were calculated. With this, pressures

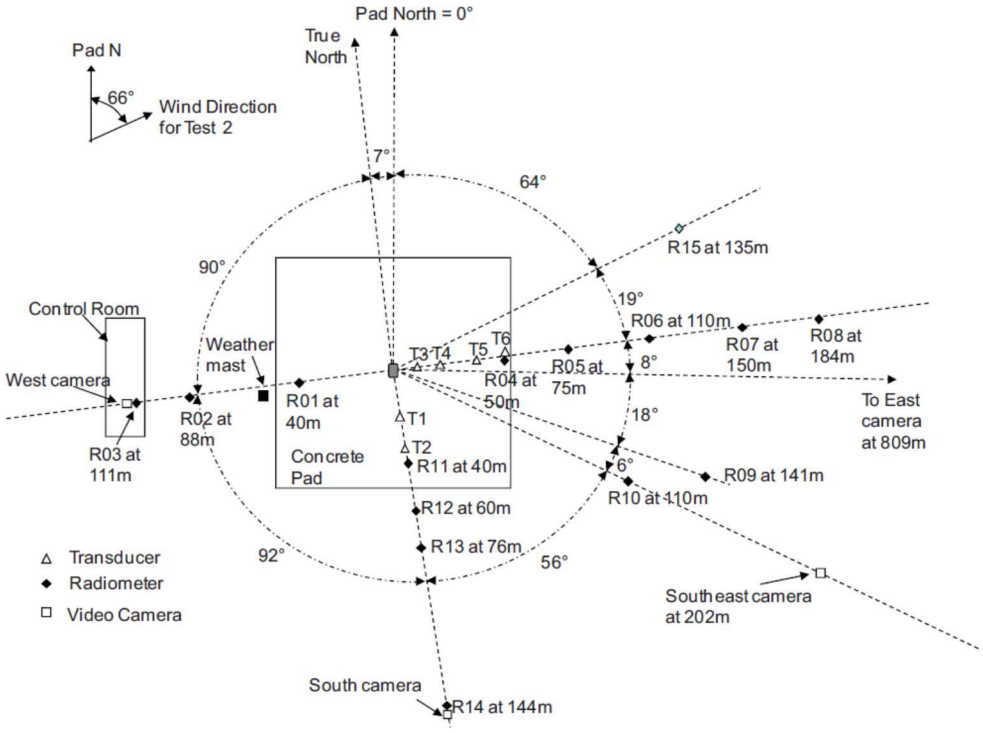

Figure 6-7 Schematic of instrumentation arrangement [22].

Table 6-5 Simulation input parameters for experiments of Lowesmith and Hankinson [22].

Parameter	Value	Unit
Discharge Coefficient (C_d)	1.0	N/A
Ambient Pressure (P_a)	1.0	bar
Ambient Temperature (T_a)	276.65	K
Initial Gas Temperature (T_g)	281.25	K
Internal Diameter (d)	150.0	mm
Initial Gas Pressure (P_g)	70	bar
Release Angle (θ)	90	deg
Relative Humidity (RH)	88	%
Radiometer Height (h_r)	1.5	m

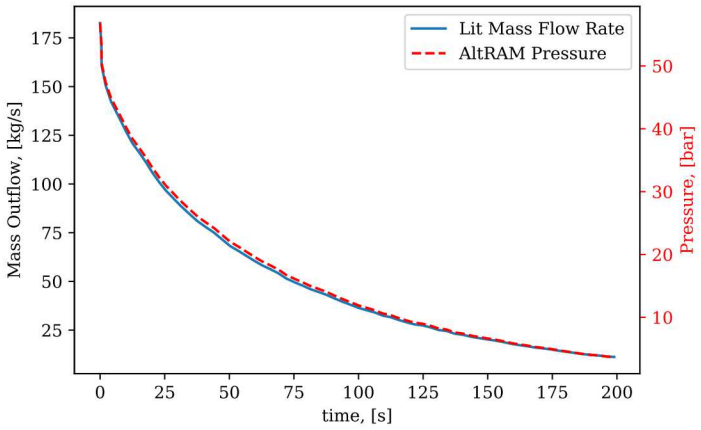

Figure 6-8 Mass flow and resultant gas pressure against release time. Lit refers to reported mass flow rate in Lowesmith et al. [22].

values were interpolated to match the corresponding time at which experimental measurements were taken. The time dependent pressure and mass flow rates are shown in Fig. 6-8.

6.3.3. Result Comparison

Thermal radiation with respect to radial distance and cardinal direction were reported. These measurements were recorded at times 20, 60, and 100 s. Since AltRAM radial profiles are axis-symmetric, one profile was used to compare to all experimental sets. Pressure values at the corresponding times were interpolated from the data shown in Fig. 6-8. Figure 6-9 display the compared thermal radiation levels. First note the wind direction shown in Fig. 6-7. Due to the north eastern wind direction, Lowesmith and Hankinson reported the south, south eastern readings as "wind neutral". For these cardinal directions the model is in good agreement with the experimental data. The magnitude of values as well as the steepness of slope are much higher in the eastern readings due to the interference of wind. The under-prediction of thermal radiation in the wind effected direction (east) is counter to what was reported in Sections 6.1.3 and 6.2.3. Note that unlike the comparisons in Sections 6.1 and 6.2 where heat flux was over-predicted for horizontal or 45° flames, the jet flame trajectory in this case was vertically upwards.

Lowesmith also reported the measured Radiant Fraction (X_r) of the jet flame against time. A multipoint computation was utilized and the standard deviation between the points of measurements are shown along with the simulated values in Fig. 6-10. The experimental radiant fractions are higher than those calculated by AltRAM. Since a multipoint method was used and a denser population of radiometers were located downwind compared to upwind, the experimental measurements may have been shifted higher.

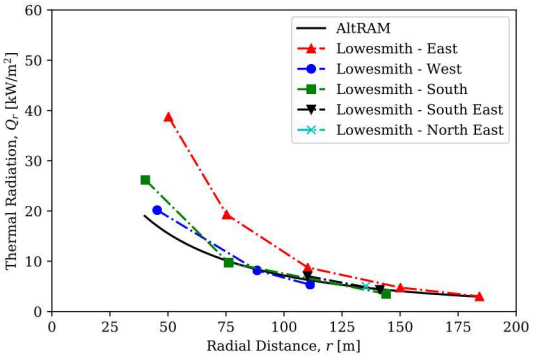

(a) 20 seconds.

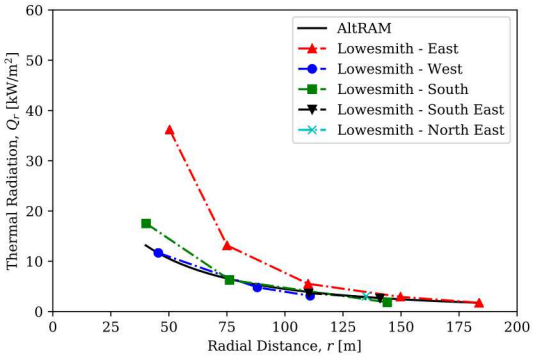

(b) 60 seconds.

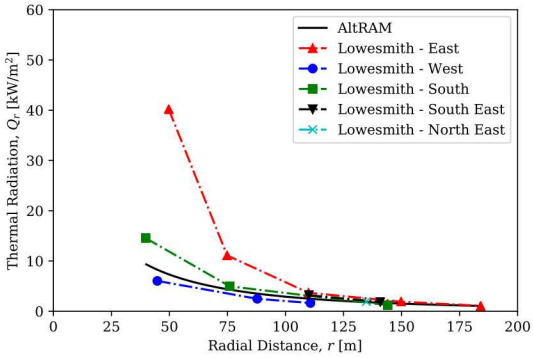

(c) 100 seconds.

Figure 6-9 Thermal radiation versus radial distance as different cardinal directions at different times. Lowesmith label refers to Lowesmith et al. [22].

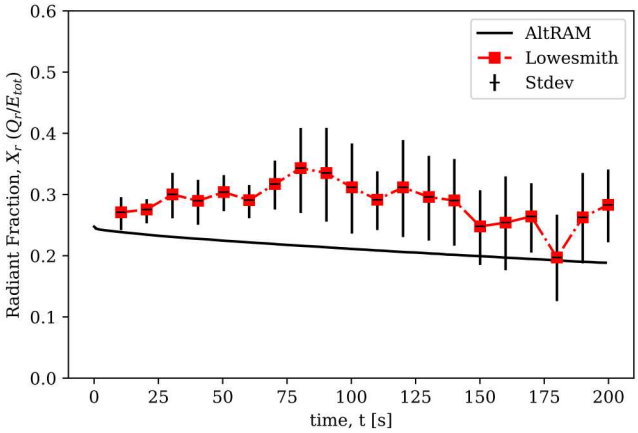

Figure 6-10 Radiant fraction versus time. Lowesmith refers to Lowesmith et al. results [22].

Table 6-6 Wind conditions.

Wind measurement	test 1	test 2	test 3	unit
Velocity	0.3	3.9	6.9	m/s
Direction	326 (NW)	271 (W)	269 (W)	° from N

Table 6-7 Simulation input parameters for experiments of Johnson et al. [23].

Parameter (symbol)	test 1	test 2	test 3	unit
Internal Diameter (d)	152	75	20	mm
Discharge Coefficient (C_d)	0.85	0.85	0.85	N/A
Ambient Temperature (T_a)	281	282	286	K
Ambient Pressure (P_a)	1.0	1.0	1.0	bar
Gas Storage Temperature (T_g)	267	279	281	K
Gas Storage Pressure (P_g)	3.0	12.1	67.1	bar
Relative Humidity (RH)	0.80	0.81	0.91	-

6.4. Johnson et al. (1994) [23]

In "A Model for Predicting the Thermal Radiation Hazards from Large-Scale Horizontally Released Natural Gas Jet Fires," Johnson et al. [23] describe large scale underexpanded NG jet flames. Thermal radiation was measured for these horizontal flames. The experiments were conducted out doors at British Gas test site Spadeadam in Cumbria.

6.4.1. Experimental Details

Three large scale underexpanded jet flames released and observed. The experimental gas composition was reported as 94% methane. The flame releases were 3.2 or 1.7 m above ground level. The source diameter ranged from 20 to 152 mm with a reported discharge coefficient $C_d = 0.85$. All releases were conducted outside with wind speeds ranging from 0.3 to 6.9 m/s. Wind traveled in between the north and west cardinal directions, specific values are reported per experimental release as listed in Table 6-6. All reported experimental values were average over 10 to 20 seconds. The mass flow rate was calculated using an isotropic flow equation from pressure and temperature measurements taken 400 mm upstream of the release point.

6.4.2. Simulation Description

As stated above three large scale jet flames were simulated for AltRAM validation. The specific experimental parameter used to construct the simulations are shown in Table 6-7. The atmospheric pressure was not reported and thus standard conditions were assumed. Additionally, all the release directions were horizontal in the eastward direction.

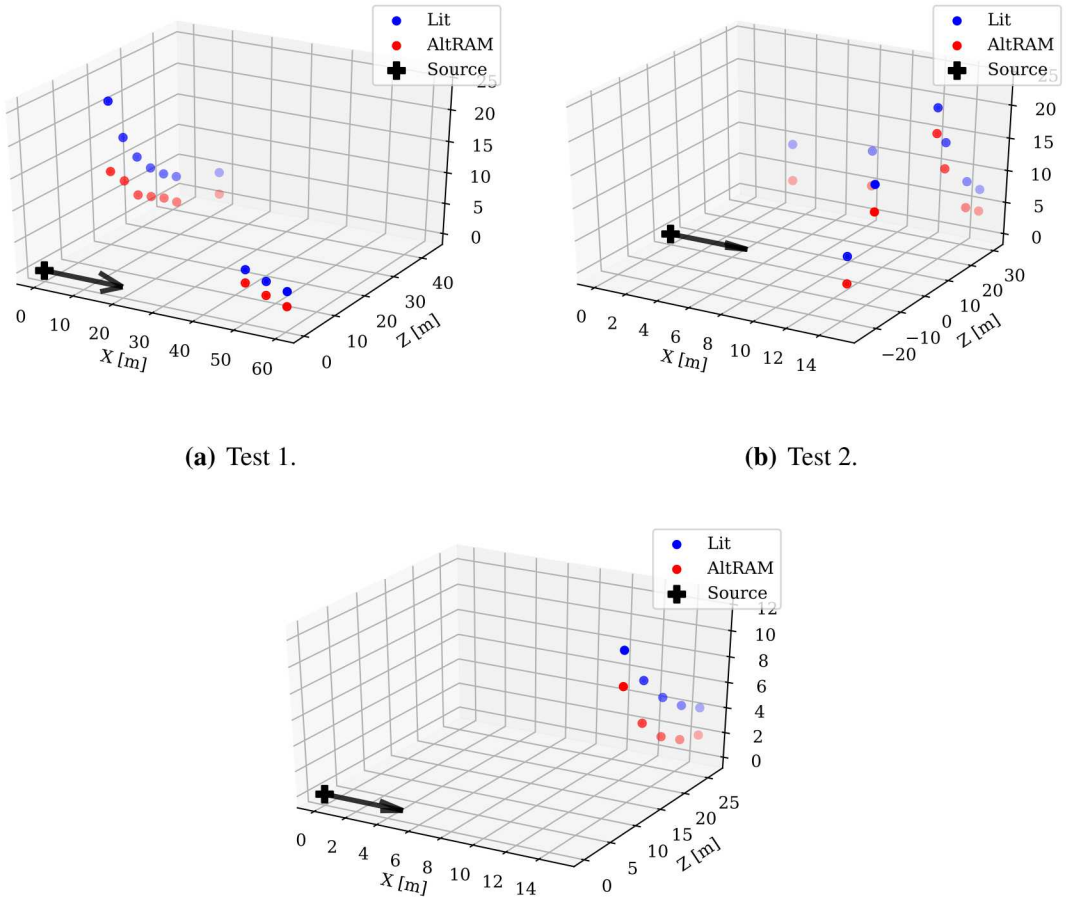

(a) Test 1.

(b) Test 2.

(c) Test 3.

Figure 6-11 Thermal radiation for all three test configurations. Lit label refers to Johnson et al. [23].

6.4.3. Result Comparison

Thermal radiation measurements at various downwind locations were reported. Modeled values are compared in Fig 6-11. The black '+' marker in Fig. 6-11 serve as a representation of the source location. The flame direction is along the x axis in all cases.

The modeled horizontal jet flames produced lower thermal radiation values for all releases. The counter flow of the wind to the release direction could contribute to the error.

7. CONCLUSIONS

Two of the physical models, for unignited dispersion and jet flames in the Alternative Fuels Risk Assessment Models (AltRAM) toolkit are described in this work. There are several submodels to describe the flow or flame: a model for flow through an orifice, a notional nozzle model (if the flow is choked), a flow establishment model where a plug flow develops into a Gaussian turbulent diffusion flow, and finally, an unignited dispersion or jet flame model.

Validation of these two models for natural gas was carried out by simulating the experiments of trusted sources. The reported experimental parameters were used as inputs. Missing information about key experimental details were dealt with by justifiable assumptions or in some cases, abandonment of the experiment.

Within Sections 3 and 4, three sub-sonic releases and 17 underexpanded jets were simulated and the unignited dispersion of natural gas was compared to AltRAM. For the centerline concentration of underexpanded jets, the predicted values are in good agreement with the wide range of experimental results. For subsonic releases, the near-field concentration predictions are in good agreement with the data, but the AltRAM model tends to under-predict the concentration in the far-field slightly, potentially due to the empirical entertainment model in the buoyancy dominated regions of the flow. Some simulations not shown in this work improved the agreement in the far-field by adjusting the entrainment constant.

Within Sections 5 and 6, the validation of AltRAM's jet flame models are discussed. The validation was carried out by modeling the experiments of trusted and well documented natural gas jet flames. The reported experimental parameters were used to initialize AltRAM in order to model experimental results. Missing information of key experimental conditions were filled in with justifiable assumptions. From the literature it was noted that most large-scale flame studies occur outdoors due to safety or facility constraints. Therefore, the cross or co-flow of wind is suspected to be a source of error; AltRAM currently does not take these effects into account.

A total of nine underexpanded jet flames were evaluated as well as one subsonic flame, as described in Sections 5 and 6. The overall trend for underexpanded jets was an over-prediction of radiative heat fluxes. Of the nine underexpanded releases only one was oriented vertically (see Section 6.3). For the wind neutral directions as reported by Lowesmith and Hankinson [22] AltRAM's prediction matched the experimental results. The other vertical release was the subsonic flame but with co-flowing air; only the release described by Lowesmith and Hankinson [22] is representative AltRAMs models. Therefore, effects which contribute more heavily in horizontal releases (e.g. buoyancy) may be responsible for the over-prediction in the radiative heat flux.

For the horizontal release described in Lowesmith and Hankinson [20], images from the experiment of the flame engulfing the pipe were displayed in Section 6.1.3. The temperature contours produced by AltRAM showed that the lift off of the simulated flame was significantly over-predicted. As with the overprediction in heat flux, this could be due to the buoyancy model.

Further investigation could also be made on the lift-off distance of the flame. As noted in the experiment of Hankison et al. [19], for the horizontal release a stable flame was formed approximately 10 m downstream of the release point. The engineering zones used to represent the jet expansion provide a pseudo un-ignited region but it might not provide an adequate downstream distance. This could be a potential explanation for the under-predicted near field values and over-predicted far field values seen in Section 4.1.

AltRAM has been shown to be a reasonably accurate tool for calculating the concentration or flame properties of natural gas releases. These models can provide valuable information for the risk assessment of natural gas infrastructure.

REFERENCES

[1] W. G. Houf and R. W. Schefer. “Analytical and experimental investigation of small-scale unintended releases of hydrogen”. *Int. J. Hydrogen Energy* 33 (2008), 1435–1444.

[2] W. S. Winters and W. G. Houf. “Simulation of small-scale releases from liquid hydrogen storage systems”. *Int. J. Hydrogen Energy* 36 (2011), 3913–3921.

[3] W. Houf and W. Winters. “Simulation of high-pressure liquid hydrogen releases”. *Int. J. Hydrogen Energy* 38 (2013), 8092–8099.

[4] I. Ekoto, a.J. Ruggles, L. Creitz, and J. Li. “Updated jet flame radiation modeling with buoyancy corrections”. *Int. J. Hydrogen Energy* 39 (2014), 20570–20577.

[5] I. H. Bell, J. Wronski, S. Quoilin, and V. Lemort. “Pure and Pseudo-pure Fluid Thermophysical Property Evaluation and the Open-Source Thermophysical Property Library CoolProp”. *Industrial & Engineering Chemistry Research* 53 (2014), 2498–2508. eprint: http://pubs.acs.org/doi/pdf/10.1021/ie4033999.

[6] U. Setzmann and W. Wagner. “A New Equation of State and Tables of Thermodynamic Properties for Methane Covering the Range from the Melting Line to 625 K at Pressures up to 100 MPa”. *Journal of Physical and Chemical Reference Data* 20 (1991), 1061–1155. eprint: https://doi.org/10.1063/1.555898.

[7] K. B. Yüceil and M. V. Ötügen. “Scaling parameters for underexpanded supersonic jets”. *Physics of Fluids* 14 (2002), 4206–4215.

[8] A. D. Birch, D. J. Hughes, and F. Swaffield. “Velocity Decay of High Pressure Jets”. *Combustion Science and Technology* 52 (1987), 161–171. eprint: http://www.tandfonline.com/doi/pdf/10.1080/00102208708952575.

[9] A. D. Birch, D. R. Brown, M. G. Dodwon, and F. Swaffield. “The Structure and Concentration Decay of High Pressure Jets of Natural Gas”. *Combust. Sci. Technol.* 36 (1984), 249–261.

[10] B. C. R. Ewan and K. Moodie. “Structure and Velocity Measurements in Underexpanded Jets”. *Combustion Science and Technology* 45 (1986), 275–288. eprint: http://dx.doi.org/10.1080/00102208608923857.

[11] V. Molkov, D. Makarov, and M. Bragin. “Physics and modelling of under-expanded jets and hydrogen dispersion in atmosphere”. In: *Proceedings of the 24th international conference on interaction of intense energy fluxes with matter*. 2009.

[12] W. S. Winters. *Modeling Leaks from Liquid Hydrogen Storage Systems*. Tech. rep. SAND2009-0035. 2009.

[13] C. D. Richards and W. M. Pitts. “Global density effects on the self-preservation behaviour of turbulent free jets”. *J. Fluid Mech.* 254 (1993), 417–435.

[14] C. J. Chen and W. Rodi. *Vertical turbulent buoyant jets: a review of experimental data*. 1980.

[15] H. B. Fischer, E. J. List, R. C. Koh, J. Imberger, and N. H. Brooks. *Mixing in Inland and Coastal Waters*. San Diego: Academic Press, 1979.

[16] A. D. Birch, D. R. Brown, M. G. Dodson, and J. R. Thomas. “The turbulent concentration field of a methane jet”. *J. Fluid Mech.* 88 (1978), 431–449.

[17] A. D. Birch, D. R. Brown, D. K. Cook, and G. K. Hargrave. “Flame Stability in Underexpanded Natural Gas Jets”. *Combust. Sci. Technol.* 58 (1988), 267–280.

[18] E. Brennan, D. Brown, and M. Dodson. “Dispersion of high pressure jets of natural gas in the atmosphere”. In: *Symp. Protection of Exothermic Reactors & Pressurised Storage Vessels*. 1984.

[19] G. Hankinson, B. J. Lowesmith, P. Genillon, and G. Hamaide. “Experimental Studies of Releases of High Pressure Natural Gas From Punctures and Rips in Above-Ground Pipework”. In: *Vol. 1 Codes, Stand. Regul. Des. Constr. Environ. GIS/Database Dev. Innov. Proj. Emerg. Issues*. Vol. 1. ASME, 2000, V001T01A009.

[20] B. J. Lowesmith and G. Hankinson. “Large scale high pressure jet fires involving natural gas and natural gas/hydrogen mixtures”. *Process Saf. Environ. Prot.* 90 (2012), 108–120.

[21] S. Baillie, M. Caulfield, D. K. Cook, and P. Docherty. “A phenomenological model for predicting the thermal loading to a cylindrical vessel impacted by high pressure natural gas jet fires”. *Process Saf. Environ. Prot.* 76 (1998), 3–13.

[22] B. Lowesmith and G. Hankinson. “Large scale experiments to study fires following the rupture of high pressure pipelines conveying natural gas and natural gas/hydrogen mixtures”. *Process Saf. Environ. Prot.* 91 (2013), 101–111.

[23] A. Johnson, H. Brightwell, and A. Carsley. “A model for predicting the thermal radiation hazards from large-scale horizontally released natural gas jet fires”. *Process safety and environmental protection* 72 (1994), 157–66.

DISTRIBUTION

Email—External

Name	Company Email Address	Company Name
Dennis Smith	Dennis.A.Smith@ee.doe.gov	Department of Energy
Mark Smith	mark.smith@ee.doe.gov	Department of Energy
Cyrus Jordan	cjjordan@ncsu.edu	North Carolina State University

Email—Internal

Name	Org.	Sandia Email Address
Ethan Hecht	8367	ehecht@sandia.gov
Myra Blaylock	8751	mlblayl@sandia.gov
Jon Zimmerman	8367	jzimmer@sandia.gov
Cheryl Lam	8751	clam@sandia.gov
Chris LaFleur	8854	aclafle@sandia.gov
Brian Ehrhart	8854	bdehrha@sandia.gov
CA Technical Library	8551	cateclib@sandia.gov

Sandia National Laboratories is a multimission laboratory managed and operated by National Technology & Engineering Solutions of Sandia LLC, a wholly owned subsidiary of Honeywell International Inc., for the U.S. Department of Energy's National Nuclear Security Administration under contract DE-NA0003525.